



Article

Hydrothermal Synthesis of SnO₂ Nanoneedle-Anchored NiO Microsphere and its Gas Sensing Performances

Zhijie Wei ¹, Qu Zhou ^{1,2,*} , Jingxuan Wang ¹, Zhaorui Lu ¹, Lingna Xu ¹ and Wen Zeng ^{3,*}¹ College of Engineering and Technology, Southwest University, Chongqing 400715, China² Electrical and Computer Engineering Department, Wayne State University, Detroit, MI 48202, USA³ College of Materials Science and Engineering, Chongqing University, Chongqing 400044, China

* Correspondence: zhouqu@swu.edu.cn (Q.Z.); wenzeng@cqu.edu.cn (W.Z.); Tel.: +86-130-683-05845 (Q.Z. & W.Z.)

Received: 10 June 2019; Accepted: 12 July 2019; Published: 15 July 2019



Abstract: In this study, we reported a successful synthesis of a nanocomposite based on SnO₂ nanoneedles anchored to NiO microsphere by a simple two-step hydrothermal route. The results show that the SnO₂/NiO nanocomposite-based sensor exhibits more prominent performances than the pristine NiO microsphere to NO₂ such as larger responses and more outstanding repeatability. The improved properties are mainly attributed to the p–n heterojunctions formed at the SnO₂–NiO interface, leading to the change of potential barrier height and the enlargement of the depletion layer. Besides, the novel and unique nanostructure provides large and effective areas for the surface reaction. In addition, a plausible growth mechanism and the enhanced sensing mechanism were proposed to further discuss the special nanostructure which will benefit the exploration of high-performance sensors.

Keywords: hydrothermal synthesis; semiconductor; SnO₂/NiO nanocomposite; NO₂; performances; sensing mechanism

1. Introduction

Metal-oxide semiconductor sensor, which plays an important role among the most necessary devices in our everyday life, has been extensively applied in various areas of gas analysis such as the identification of hazardous gases, the monitoring of air quality and the detection of environmental pollution [1–5]. So far, diverse metal oxides, for instance TiO₂ [6,7], ZnO [8,9], WO₃ [10,11], NiO [12,13], and SnO₂ [14,15], have received a lot of attention and been widely investigated. Among them, as a prominent p-type oxide semiconductor with a wide band-gap (3.6–4.0 eV), NiO has captured a tremendous amount of attention for the capability of gases detection due to its distinctive electronic nanostructure and excellent thermal stability [16,17]. However, traditional pristine NiO-based sensors have limited gas-sensing performances such as high working temperature, low sensitivity and unsatisfactory repeatability, which may impose restrictions on the fabrication of high-performance sensors [18]. In this regard, considerable efforts have been devoted to breaking through this limitation like morphology control [19,20], metal doping [21,22], nanocompositing [23,24] and so on. Off all the strategies, the synthesis of nanocomposites has been regarded as a desirable approach to substantially improve the performances of gas sensors [25]. Generally, for gas sensors, the route is expected to achieve the change of the nanostructure for more sufficient surface adsorption and the formation of a p–n heterojunction for more efficient electron transport. For example, Sun and his co-authors reported a facile hydrothermal synthesis of TiO₂ nanorods decorated with NiO nanoparticles, and the sensor based on the materials showed ultrahigh sensitivity towards 200 ppm acetone in comparison to that

of the pure NiO [26]. Zhu et al. synthesized hierarchical NiO/ZnO nanoflower, and the ethanol sensor based on the nanocomposite presented large gas responses and prominent repeatability due to the formation of the p–n heterojunction [27].

SnO₂ which is one of the most important oxygen-deficient n-type metal oxides that has taken a dominant position in the area of gas sensing nanomaterials owing to its excellent chemical stability [28,29]. Besides, it is generally known that SnO₂ has been proved to be a suitable oxide to form p–n or n–n heterojunction through the combination of other nanomaterials due to its small size effect [30]. Given this, the combination of SnO₂ and NiO has been considered to be an effective approach to enhance the properties [31,32]. Kim et al. successfully synthesized SnO₂–NiO composite nanoweb by a facile electrospinning route, and the fabricated sensor exhibited high response to NO₂ and C₆H₆ which benefited from the presence of the p–n heterojunction [33]. Meng et al. found that NiO–SnO₂ nanocomposite-based sensor exhibited more excellent gas-sensing performances than that of the pristine SnO₂-based sensor, including larger gas responses, lower working temperature, shorter response/recovery times and so on [34]. They believed that the enhancement was caused by the catalytic effect of NiO and the presence of a p–n heterojunction. Hitherto, although diverse SnO₂–NiO heterostructures have been synthesized with fascinating properties as mentioned above, to the best of our knowledge, nanocomposites based on a SnO₂ nanoneedle-anchored NiO microsphere for gas sensing application have rarely been reported. Hence, the design and synthesis of a novel and unique composite nanostructure is still a challenging task to enhance the sensing properties of sensors.

Herein, the SnO₂ nanoneedle-anchored NiO microsphere was triumphantly prepared by a simple two-step hydrothermal method. In the typical synthesis of SnO₂/NiO nanocomposite, the pristine NiO microsphere was firstly synthesized and the nanocomposite was obtained based on the as-synthesized microsphere. The sensors fabricated with the SnO₂/NiO nanocomposite presented higher gas responses and more prominent repeatability towards NO₂ in comparison to the pristine NiO microsphere, further demonstrating that the improvement of the gas-sensing performances is closely related to the change of the pristine nanostructure and formation of the p–n heterojunction. Besides, the long-term stability of the sensors was measured over a period of 30 days which shows that the fabricated sensors exhibit excellent stability. In addition, we also proposed a possible growth mechanism of the novel nanostructure and a possible mechanism to explain the improved sensing properties.

2. Materials and Methods

2.1. Preparation of SnO₂ Nanoneedle-anchored NiO Microsphere

All involved chemicals used to synthesize the SnO₂/NiO nanocomposite were analytical-grade grade and were obtained from Chongqing, Chuandong Chemical Reagent Co., Ltd. China and were used directly without further purification. The pristine NiO microsphere and SnO₂/NiO nanocomposite were synthesized hydrothermally.

To prepare the pristine NiO microsphere, 2 mmol NiCl₂·6H₂O was added into 30 mL deionized water and stirred in a beaker for 15 min. Subsequently, 25% NH₃·H₂O was added dropwise, adjusting the pH to about 10. Then, the mixed solution was transferred into an autoclave with a capacity of 50 mL, heated at 180 °C for 6 h. After the autoclave cooled down to room temperature, the precipitate was collected by centrifugation and then washed with deionized water and ethanol several times. The sample was dried at 60 °C overnight and then collected for characterization and subsequent hydrothermal treatment.

Furthermore, the SnO₂/NiO nanocomposite was obtained based on the sample as-synthesized above. In a typical process, the as-obtained precipitate and 0.8 mmol SnCl₄·5H₂O were dissolved into 30 ml deionized water under intense magnetic stirring for 15 min. Then, 0.6 mL ethylenediamine (EDA) and several drops of NH₃·H₂O were added into the solution. After stirring for 20 min, the mixed solution was transferred into the autoclave, sealed and kept at 180 °C for 10 h. Cooling naturally,

the precipitate was collected in the same route. Finally, the product was obtained via calcinating at 400 °C for 2 h.

2.2. Characterization

The crystallographic information of the products was collected by X-ray diffraction (XRD, Rigaku D/Max-2500 (Rigaku, Japan), Cu-K α radiation with $\lambda = 1.54$ nm) over the 2θ range of 20°–85°. The surface morphologies of the pristine oxide and composite were observed via scanning electron microscopy (SEM, JSM-7800F, JEOL, Japan). Energy dispersive spectroscopy (EDS) analysis was examined with INCA 250 (Oxford, UK). Moreover, the chemical states of the as-prepared composite were analyzed via X-ray photoelectron spectroscopy (XPS, ESCALAB-MK, VG, UK) with Al-K α as the excitation source.

2.3. Fabrication and Measurement of Gas Sensors

The gas sensor was designed with a side-heated structure (Figure 1a). Concretely, the as-prepared powder was dispersed in the water–ethanol mixed solution to form a homogeneous slurry which was coated onto an alumina ceramic tube evenly to form a sensing film. Afterwards, a pair of Au electrodes, which were connected with two Pt wires, were installed at every end of the tube. In addition, a Ni–Cr wire was inserted into the tube to change the heating current for the adjustment of the operating temperature, as shown in Figure 1b. At last, the fabricated sensor was aged at 300 °C for 2 weeks to ensure its high stability [35,36].

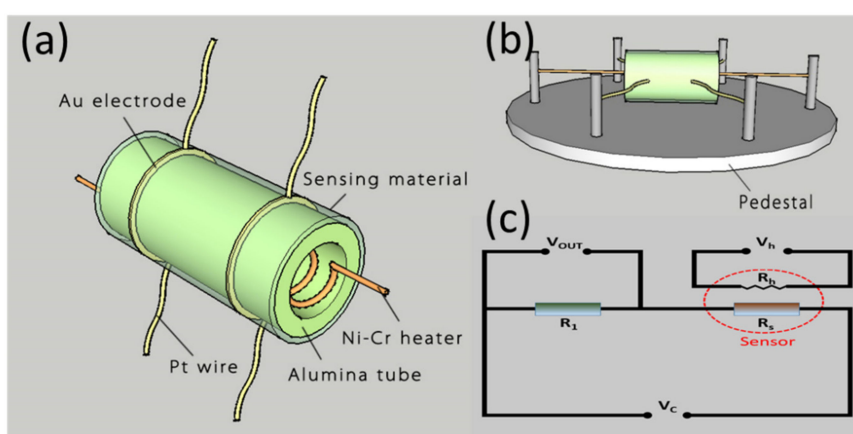


Figure 1. (a,b) Schematic illustration of the fabricated sensor. (c) Electric circuit of sensor device.

The gas-sensing properties to NO₂ were measured on a Chemical Gas Sensor-8 gas-sensing analysis system (Beijing Elite Tech Co., Ltd., Beijing, China) controlled by a central computer. As presented in Figure 1c, the working temperature of the fabricated sensor was adjusted by changing the heating voltage (V_h). The resistance of the tested sensor was calculated with the value of the output voltage (V_{out}). The sensor was put into the airtight chamber with air, and then the concentration of the target gas was controlled by the injection of a certain amount of the gas. The carrier gas of the gas-sensing analysis system is O₂, and the volume of the gas chamber is 20 L. Besides, the flux of the target gas and carrier gas is 20 ml/min. In this paper, the gas response of the fabricated sensor is defined as the ratio R_g/R_a , where R_g is the electrical resistance of the sensor in target gas and R_a the value in air [37].

3. Results and Discussion

3.1. Structural and Morphological Analysis

As demonstrated in Figure 2a, the XRD pattern was used to investigate the phase and crystalline structure of the obtained samples. From the typical pattern, it is obvious that the characteristic

peaks at 36.9° , 43.2° , 63.1° and 75.4° could be assigned to the planes of (111), (200), (220) and (311), perfectly indexing to the NiO (JCPDS 78-0423). To confirm the synthesis of the composite, it is obvious from another result that the diffraction peaks around 26.7° , 33.9° , 52.6° , and 62.0° could be indexed to (110), (101), (211), and (002) planes of the SnO₂ (JCPDS 41-1445), verifying the coexistence of SnO₂ and NiO. In addition, the high purity of the synthesized sample can be confirmed by all the sharp and clear diffraction peaks. Besides, to further observe the elemental composition of the samples, EDS analysis was carried out as seen in Figure 2b. The results indicate that the pristine sample contains O, and Ni elements and the nanocomposite contain O, Ni and Sn elements.

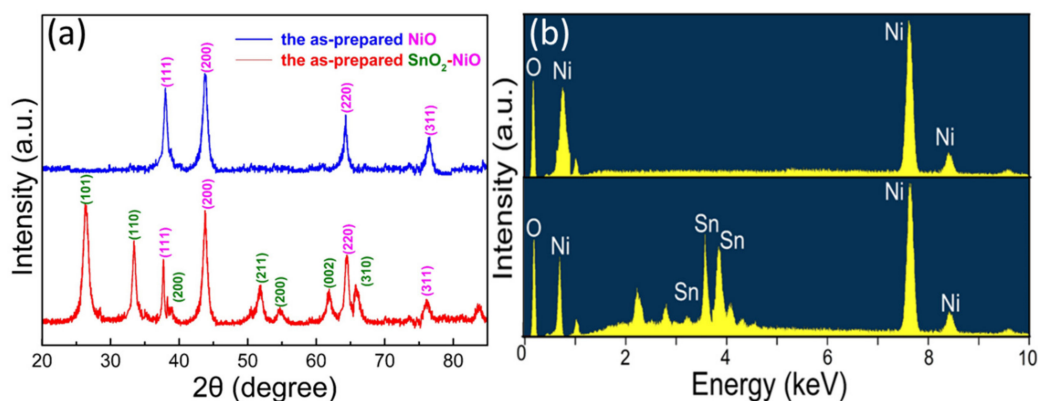


Figure 2. (a) XRD pattern of the synthesized samples. (b) EDS spectrum of the SnO₂/NiO nanocomposite.

The surface morphologies of the pristine NiO and SnO₂/NiO nanocomposite were characterized by SEM observations. As displayed in Figure 3a,c, both the samples demonstrated a sphere-like morphology with relatively regular shapes. Higher magnification SEM micrographs of the two single microspheres are illustrated in Figure 3b,d. From Figure 3b, it can be observed clearly that the microsphere has a smooth surface morphology with a uniform diameter of 2 μm . The detailed structure of the nanocomposite is demonstrated in Figure 3d and the result shows that the microsphere with the same diameter of 2 μm was anchored by numerous nanoneedles on the surface, making the morphology rough and loose which provides large and effective areas for the surface reaction.

Raman scattering was used to confirm the synthesis of NiO and study the structural transition. As shown in Figure 4, the Raman spectra of the pristine NiO and the SnO₂/NiO nanocomposite were carried out from 200 to 1400 cm^{-1} . It can be found from the pristine product that the strong and broad peak at 520 cm^{-1} can be attributed to the Ni–O stretching mode. It is generally known that the lattice distortion has an effect on the lattice parameters and cell volume, leading to the change of the Raman frequencies [38]. The results of the composite spectrum exhibited that the shift to the lower frequency side of the mode, which was caused by the introduction of Sn, suggested the synthesis of the SnO₂/NiO nanocomposite.

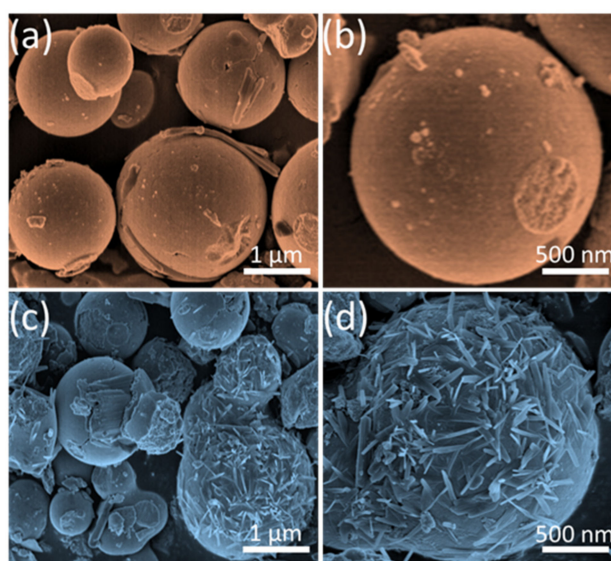


Figure 3. (a,b) SEM micrographs of the pristine NiO. (c,d) SEM micrographs of the SnO₂/NiO nanocomposite.

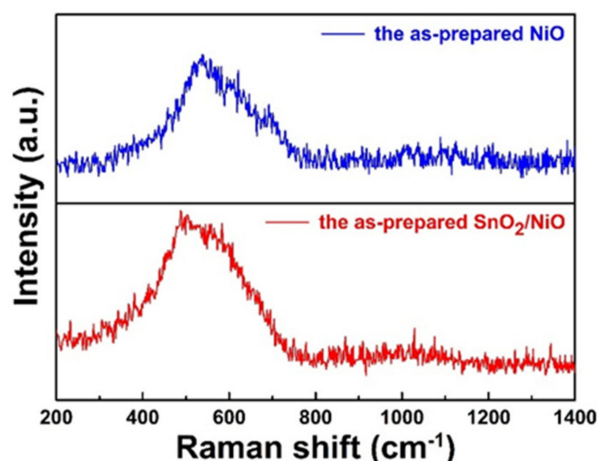


Figure 4. Raman scattering spectra of the pristine NiO and SnO₂/NiO nanocomposite.

To further investigate the chemical states and surface chemical compositions of the SnO₂/NiO nanocomposite, XPS analysis was performed as shown in Figure 5. From the full-wide (0–1000 eV) scanned survey spectrum (Figure 5a), it is obvious that the presence of Ni, O, Sn, and C in the SnO₂/NiO nanocomposite, verifying again the high-purity of the as-synthesized composite. The Ni 2p XPS spectrum can be decomposed into four peaks in Figure 5b. The peaks located at 872.7 eV and 879.6 eV can be assigned to the Ni 2p_{1/2} and its satellite, while the peaks at 855.2 eV and 861.1 eV are ascribed to Ni 2p_{3/2} and its satellite, respectively. The observed four peaks can be attributed to the Ni²⁺, suggesting the presence of NiO. Figure 5c displays the high-resolution Sn 3d spectrum, from which we can find that the two measured strong peaks are located at 495.1 eV and 486.6 eV, which can be assigned to the Sn 3d_{3/2} and Sn 3d_{5/2}, respectively. The two peaks and their spin-orbit splitting (8.5 eV) indicate the presence of Sn⁴⁺ in SnO₂. The high resolution O 1s spectrum can be deconvoluted into three peaks as shown in Figure 5d. These peaks at 529.7 eV, 530.8 eV and 532.0 eV matched well with three different O species of the composite. The O 1s peaks at 529.7 eV are affected by the defect of the crystal, and the middle binding energy (530.8 eV) is ascribed to the lattice oxygen of SnO₂/NiO nanocomposite, while the high binding energy (532.0 eV) can be assigned to the absorbed oxygen ions on the surface [34,39,40].

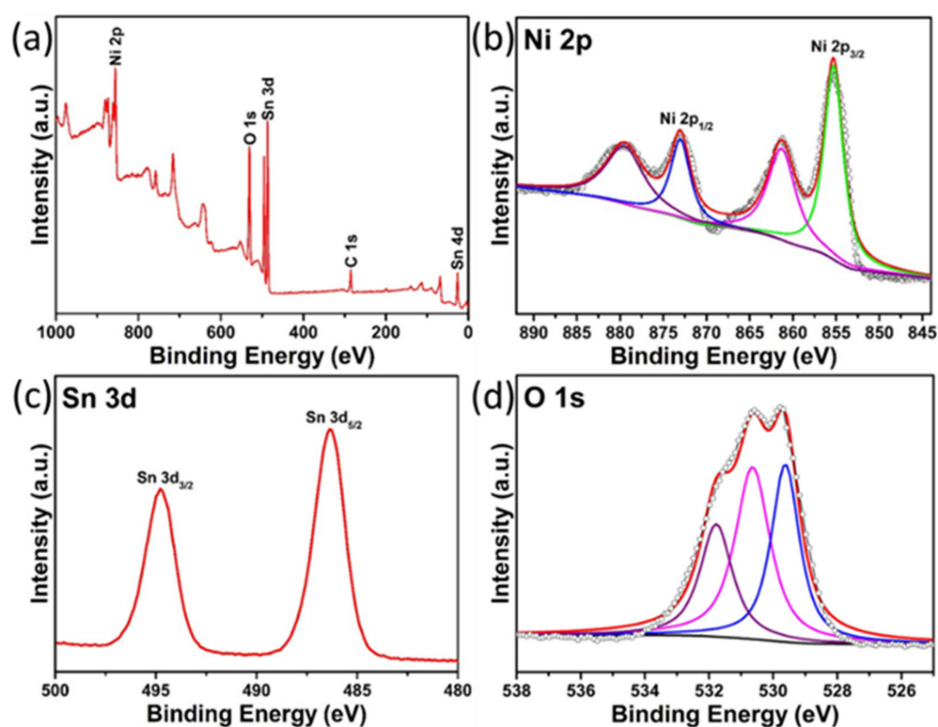


Figure 5. XPS spectra of the SnO₂/NiO nanocomposite: (a) survey spectrum; (b) Ni 2p; (c) Sn 3d; (d) O 1s.

3.2. Growth Mechanism

Based on the analysis and experimental observations, a plausible growth process of the SnO₂ nanoneedle-anchored NiO microspheres was proposed, as sketched in Figure 6. The smooth NiO microspheres were formed through the first hydrothermal treatment. First, Ni(OH)₂ nucleus was formed as a precursor, owing to Ni²⁺ reacting with OH⁻ at the initial stage of the heating process. Then, the pristine microspheres were formed with the self-assembly and had limited growth. To synthesize the SnO₂ nanoneedle-anchored NiO microspheres, EDA was added in the second hydrothermal treatment as a surfactant and nanostructure-directing agent. Specifically, the Sn(OH)₄ nucleus was developed for numerous single rods owing to the oriented effect of EDA. With the heating time increasing, the pristine rods self-aggregated to eliminate the surface energy and then formed the nanoneedles. Consequently, through continuous aggregation with the assistance of EDA and subsequent calcination, the SnO₂ nanoneedle-anchored NiO microspheres were obtained.

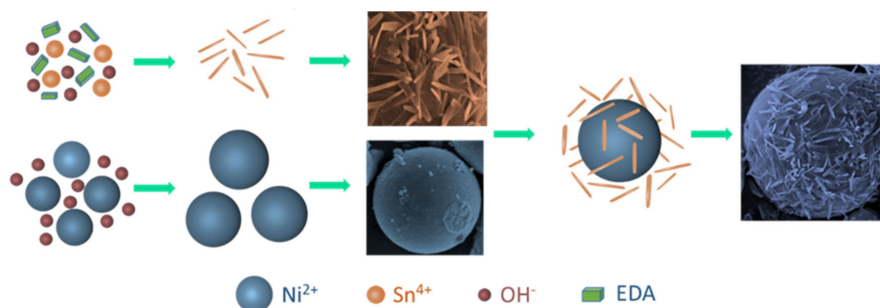


Figure 6. Schematic diagram of the possible growth mechanism of the SnO₂/NiO nanocomposite.

3.3. Gas Sensing Properties

To investigate the influence of the gas-sensing performances caused by the nanocompositing, the gas sensors were fabricated and then the NO₂ sensing performances were measured. Firstly,

the fabricated sensors based on the pristine NiO and the SnO₂/NiO nanocomposite were exposed to 20 ppm NO₂ at different temperatures (110–410 °C) to find out the optimum working temperature.

As shown in Figure 7a, the gas responses of the two sensors increased with the increasing working temperature to a certain value and then decreased with further increasing temperature. The behaviors of the temperature characteristic may be ascribed to kinetics and thermodynamics. At a lower temperature region, the low responses are caused by the high activation energy of the target gas adsorption. Besides, the active oxygen species on the material surface are limited owing to the low activation energy which can cause the transfer of electrons. With the working temperature increase, the oxygen and target gas adsorbed effectively, leading to the accelerated reaction between the active oxygen species and adsorbed target gases. During the increased temperature process, the response reaches the maximum with a certain temperature and the condition may be regarded as a balance of the adsorption and desorption. When the working temperature further increased, the balance was broken and the responses were decreased due to the increased desorption rate, resulting in the escape of target gases before effectively adsorbing on the material surface. In this work, the more obvious behavior and higher responses of the SnO₂/NiO nanocomposite can be observed, and the result can be attributed to its rough and loose morphology which provides large and effective areas for the surface reaction. It is worth noting that the optimum working temperatures of the two samples are 320 °C and 230 °C, whose corresponding responses are 3.03 and 14.45, respectively.

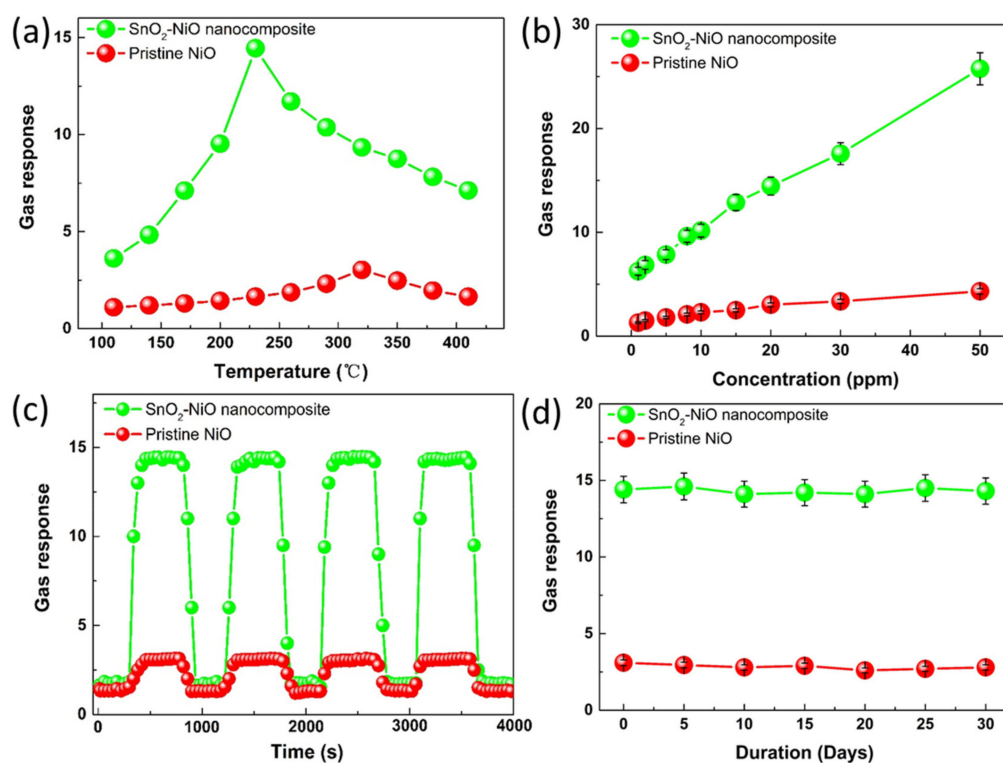


Figure 7. (a) The gas responses of the two samples to 20 ppm NO₂ at various working temperatures. (b) The gas responses of the two samples towards various concentration of NO₂ at the optimum temperature of 230 °C. (c) The dynamic responses of the two samples at the optimum temperature of 230 °C under 20 ppm NO₂. (d) The stability of the two samples towards 20 ppm NO₂ at the optimum temperature of 230 °C.

Then, Figure 7b depicts the gas responses of the two sensors towards different concentrations of NO₂ (1–50 ppm) at their own optimum temperature. It can be found that the responses of the two sensors increased obviously linearly with the increasing NO₂ concentration in the tested

range. In addition, it is also worth noting that the responses of the sensor based on the SnO₂/NiO nanocomposite exhibit a more excellent performance than the pristine NiO.

Moreover, the response–recover curves towards 20 ppm NO₂ at the optimum working temperatures were measured to ensure the repeatability. It can be seen from the result (Figure 7c) that the response of the two sensors goes up rapidly when NO₂ is in but returns to the initial condition when the gas is out. The result shows that the fabricated sensors have excellent repeatability after four reversible cycles. The measured gas-sensing performances verify again that the sensor based on the nanocomposite shows higher responses than the pristine NiO. The response and recovery characteristics of the two sensors further demonstrate that the nanocomposite based on SnO₂ nanoneedles anchored to the NiO microsphere is relatively more sensitive to NO₂ than the NiO microsphere. As discussed above, the SnO₂/NiO nanocomposite may be a potential material for sensing application as compared to the pristine NiO.

To confirm the long-term stability of the NO₂ sensors, further responses were measured over a period of 30 days, as displayed in Figure 7d. The gas-sensing properties of the two sensors to 20 ppm NO₂ at their own optimum temperature were tested every 5 days. The result shows that the fabricated sensors exhibit excellent stability with inapparent drift of responses.

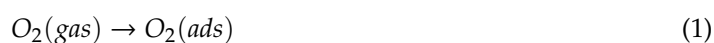
Besides, NO₂ sensing characteristics of the SnO₂/NiO nanocomposite compared with some reported nanomaterials are listed in Table 1, from which we can find that the obtained SnO₂/NiO nanocomposite in the present work shows more excellent NO₂ responses than those reported papers because of the change of nanostructure and the formation of the p–n heterojunction.

Table 1. Comparison of different NO₂ sensors.

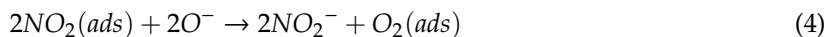
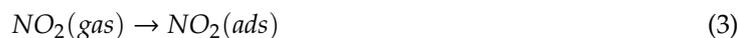
Materials	Concentration (ppm)	Operating Temperature (°C)	Response	Ref.
WO ₃ nanorods/graphene nanocomposites	1	300	5	[41]
Ppy–WO ₃ nanocomposites	100	R.T.	1.61	[42]
PTSA doped Ag-PPy nanocomposites	100	R.T.	1.68	[43]
Ni@ZnO/PANi nanocomposites	100	R.T.	1.75	[44]
WO ₃ –In ₂ O ₃ nanocomposites	1	140	2	[45]
SnO ₂ /NiO nanocomposites	20	230	14.45	This work

3.4. Gas Sensing Mechanism

It is known that the change of electric resistance caused by the reaction between adsorbed oxygen species and tested gases are used to demonstrate the basic gas-sensing mechanism [46]. Before the injection of NO₂, the oxygen molecules have adsorbed on the materials because of their strong electronegativity. During the process, the electrons in the conduction band were captured and then the oxygen molecules were reduced to chemisorbed oxygen ions which are O²⁻ (below 100 °C), O⁻ (100–400 °C) and O₂⁻ (above 400 °C) [47]. Generally, when the electrons transfer from the oxides to the chemisorbed oxygen ions, the electron concentration of the oxides on the surface decreases obviously. For p-type NiO, the adsorption of oxygen molecules is promoted by the capturing of electrons from the valance band, leading to a holes accumulation layer and a low resistance in comparison to the core regions. On the contrary, n-type SnO₂ shows a different behavior. Because of the transfer of conduction band electrons, a depletion layer can be formed on the surface of the metal oxides which will make the resistance increase. The oxygen chemisorption process can be described as follows [40]:



When NO_2 molecules were injected, the oxidizing target molecules reacted with chemisorbed oxygen ions. With higher electron affinity compared with adsorbed oxygen, NO_2 molecules extract more electrons, as shown in the following relations:



Besides, to further understand the enhanced properties caused by the formation of p–n heterojunctions, the sensing behaviors of pristine NiO and SnO_2/NiO nanocomposite were investigated. As discussed above, when pristine NiO sensing materials are exposed to air, the oxygen molecules will adsorb on the surface and be ionized into O^- , as depicted in Figure 8a. Figure 8b presents the sensing process and reaction of the pristine NiO-based sensor in NO_2 . In particular, in the case of the SnO_2/NiO nanocomposite, the p–n heterojunctions are formed at the interface between the n-type SnO_2 and n-type NiO with their different bandgap and Fermi Level which are caused by the charge carriers transport. The appearance of the heterojunctions cause the formation of the barrier and generate a depletion region. Specifically, as seen in Figure 8c, when the nanocomposite was exposed to air, the p–n heterojunctions made the fabricated sensor display a much higher electric resistance than the pristine sensor during the oxygen ionization process. When NO_2 molecules were injected (Figure 8d), the target molecules reacted with adsorbed oxygen ions with a release of numerous trapped electrons, causing an obvious shrinkage of the p–n heterojunction depletion region [27,48]. Consequently, the obvious improved gas-sensing performances were observed due to the dramatic change of the sensor resistance.

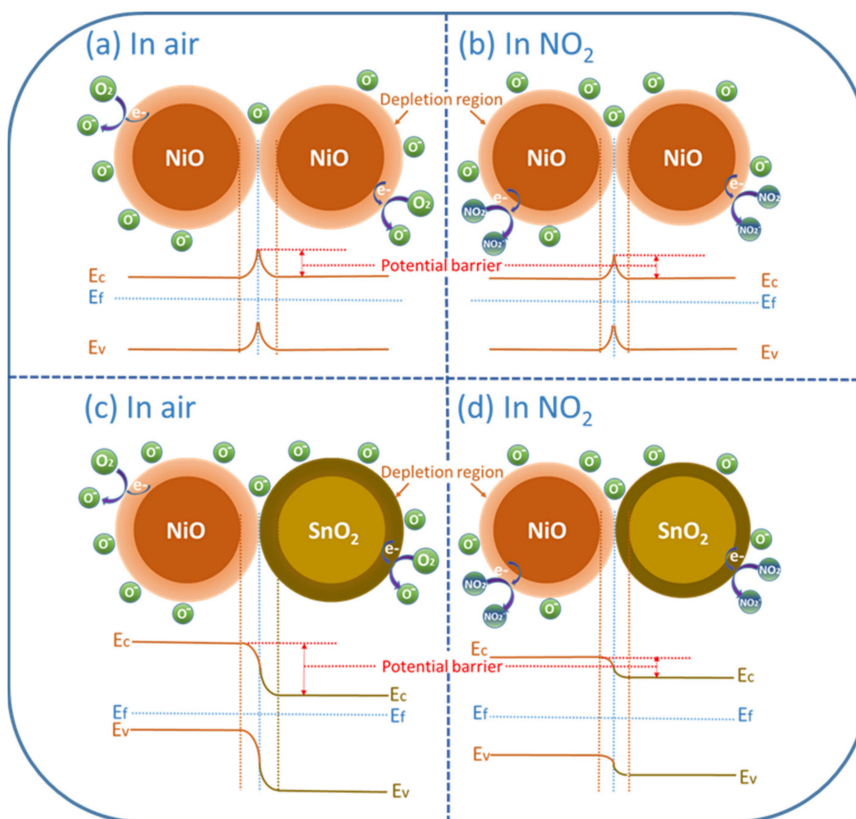


Figure 8. The sensing mechanism of (a,b) pristine NiO and (c,d) SnO_2/NiO nanocomposite.

On the other hand, it is generally known that the surface morphology plays an important role in the gas-sensing process. In this work, the novel and unique structure of the SnO_2/NiO

nanocomposite was discussed in comparison to the pristine NiO. As shown in the SEM micrographs above, the result shows that the pristine NiO microsphere has a smooth surface while the nanocomposite has a rough surface based on SnO₂ nanoneedles anchored to the NiO microsphere. More specifically, the NiO microsphere with a smooth surface possesses limited surface area for the oxygen and target gas molecules, indicating that the sensor exhibits lower response, as displayed in Figure 9a. On the contrary, the structure in Figure 9b possesses numerous nanoneedles on the surface, which provides numerous adsorption and desorption sites to the molecules. Besides, the rough surface increases the residence time of the molecules, leading to adequate surface reaction.

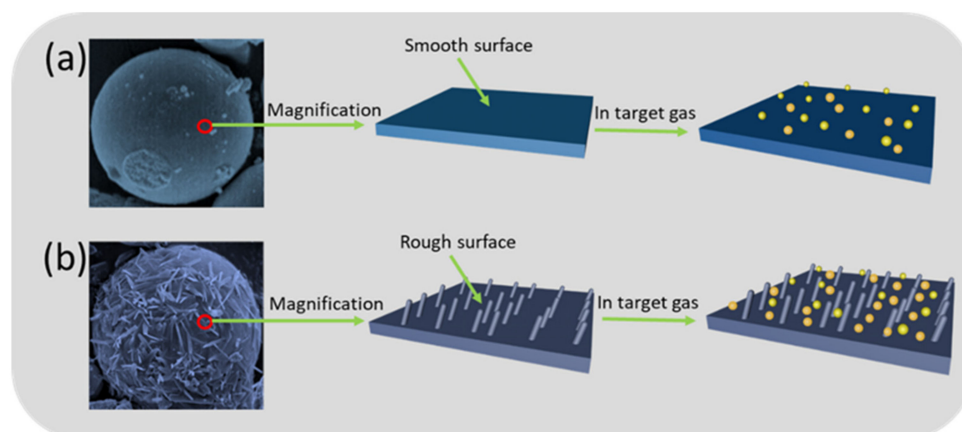


Figure 9. Schematic illustrations of the sensing mechanism. (a) The sensing mechanism of smooth surface. (b) The sensing mechanism of rough surface.

4. Conclusions

In summary, a novel nanocomposite based on SnO₂ nanoneedles anchored to NiO nanosphere has been successfully obtained via a simple two-step hydrothermal method. The sensor fabricated with the SnO₂–NiO nanocomposite exhibited prominent repeatability and much larger gas response (14.45) in comparison to the pristine NiO to 20 ppm NO₂ at its optimum working temperature of 230 °C. The improved gas-sensing properties were discussed with a possible growth process and gas sensing mechanism, indicating that the enhancement was attributed to the change of nanostructure for more sufficient surface adsorption and the formation of a p–n heterojunction for more efficient electron transport.

Author Contributions: Conceptualization, Z.W. and Q.Z.; methodology, Z.W. and Q.Z.; validation, J.W., Z.L. and L.X.; investigation, Z.W. and J.W.; resources, L.X.; data curation, Z.W.; writing—original draft preparation, Z.W.; writing—review and editing, Z.W., Q.Z. and W.Z.; visualization, Z.L.; supervision, Q.Z.; project administration, Q.Z. and W.Z.

Funding: This research was funded by the National Natural Science Foundation of China (No. 51507144), Fundamental Research Funds for the Central Universities (No. XDJK2019B021), the Chongqing Science and Technology Commission (CSTC) (No. cstc2016jcyjA0400), the project of China Scholarship Council (CSC) and Fundamental Research Funds for the Central Universities (No. 2019CDJGFCL001 and XDJK2019B021).

Conflicts of Interest: The authors declare no conflict of interest.

References

1. Zhang, X.X.; Dong, X.C.; Gui, Y.G. Theoretical and experimental study on competitive adsorption of SF₆ decomposed components on Au-modified anatase (101) surface. *Appl. Surf. Sci.* **2016**, *387*, 437–445. [[CrossRef](#)]
2. Zhang, D.Z.; Jiang, C.X.; Li, P.; Sun, Y.E. Layer-by-layer self-assembly of Co₃O₄ nanorod-decorated MoS₂ nanosheet based nanocomposite toward high performance ammonia detection. *ACS Appl. Mater. Inter.* **2017**, *9*, 6462–6471. [[CrossRef](#)] [[PubMed](#)]

3. Zhou, Q.; Chen, W.G.; Xu, L.N.; Kumar, R. Pt nanoparticles decorated SnO₂ nanoneedles for efficient CO gas sensing applications. *Sens. Actuators B-Chem.* **2018**, *256*, 656–664. [[CrossRef](#)]
4. Zhang, X.X.; Gui, Y.G.; Dong, X.C. Preparation and application of TiO₂ nanotube array gas sensor for SF₆-insulated equipment detection: A review. *Nanoscale Res. Lett.* **2016**, *11*, 302. [[CrossRef](#)] [[PubMed](#)]
5. Zhang, D.Z.; Wu, Z.L.; Zong, X.Q. Flexible and highly sensitive H₂S gas sensor based on in-situ polymerized SnO₂/rGO/PANI ternary nanocomposite with application in halitosis diagnosis. *Sens. Actuators B-Chem.* **2019**, *289*, 32–41. [[CrossRef](#)]
6. Liang, Y.; Yang, Y.; Zhou, H.; Zou, C.W.; Xu, K.; Luo, X.F.; Yu, T.; Zhang, W.; Liu, Y.T.; Yuan, C.L. A systematic study on the crystal facets-dependent gas sensing properties of anatase TiO₂ with designed {010}, {101} and {001} facets. *Ceram. Int.* **2019**, *45*, 6282–6290. [[CrossRef](#)]
7. Chinh, N.D.; Kim, C.; Kim, D. UV-light-activated H₂S gas sensing by a TiO₂ nanoparticulate thin film at room temperature. *J. Alloy. Compd.* **2019**, *778*, 247–255. [[CrossRef](#)]
8. Zhao, G.D.; Xuan, J.Y.; Liu, X.L.; Jia, F.C.; Sun, Y.P.; Sun, M.L.; Yin, G.C.; Liu, B. Low-Cost and High-Performance ZnO Nanoclusters Gas Sensor Based on New-Type FTO Electrode for the Low-Concentration H₂S Gas Detection. *Nanomaterials* **2019**, *9*, 435. [[CrossRef](#)]
9. Zhou, Q.; Chen, W.G.; Xu, L.N.; Peng, S.D. Hydrothermal Synthesis of Various Hierarchical ZnO Nanostructures and Their Methane Sensing Properties. *Sensors* **2013**, *13*, 6171–6182. [[CrossRef](#)]
10. Zhang, Y.X.; Zeng, W.; Li, Y.Q. NO₂ and H₂ sensing properties for urchin-like hexagonal WO₃ based on experimental and first-principle investigations. *Ceram. Int.* **2019**, *45*, 6043–6050. [[CrossRef](#)]
11. Xu, Y.Z.; Zeng, W.; Li, Y.Q. A novel seawave-like hierarchical WO₃ nanocomposite and its ammonia gas properties. *Mater. Lett.* **2019**, *248*, 86–88. [[CrossRef](#)]
12. Zhou, Q.; Umar, A.; Sodki, E.; Amine, A.; Xu, L.N.; Gui, Y.G.; Ibrahim, A.A.; Kumar, R.; Baskoutas, S. Fabrication and characterization of highly sensitive and selective sensors based on porous NiO nanodisks. *Sens. Actuators B-Chem.* **2018**, *259*, 604–615. [[CrossRef](#)]
13. Wei, Z.J.; Zhou, Q.; Wang, J.X.; Gui, Y.G.; Zeng, W. A novel porous NiO nanosheet and its H₂ sensing performance. *Mater. Lett.* **2019**, *245*, 166–169. [[CrossRef](#)]
14. Guan, X.F.; Wang, Y.J.; Luo, P.H.; Yu, Y.L.; Chen, D.G.; Li, X.Y. Incorporating N Atoms into SnO₂ Nanostructure as an Approach to Enhance Gas Sensing Property for Acetone. *Nanomaterials* **2019**, *9*, 445. [[CrossRef](#)] [[PubMed](#)]
15. Zhou, Q.; Chen, W.G.; Xu, L.N.; Kumar, R.; Gui, Y.G.; Zhao, Z.Y.; Tang, C.; Zhu, S.P. Highly sensitive carbon monoxide (CO) gas sensors based on Ni and Zn doped SnO₂ nanomaterials. *Ceram. Int.* **2018**, *44*, 4392–4399. [[CrossRef](#)]
16. Yu, K.L.; Hu, J.X.; Li, X.H.; Zhang, L.C.; Lv, Y. Camellia-like NiO: A novel cataluminescence sensing material for H₂S. *Sens. Actuators B-Chem.* **2019**, *288*, 243–250. [[CrossRef](#)]
17. Zhang, S.S.; Li, Y.W.; Sun, G.; Zhang, B.; Wang, Y.; Cao, J.L.; Zhang, Z.Y. Enhanced methane sensing properties of porous NiO nanosheets by decorating with SnO₂. *Sens. Actuators B-Chem.* **2019**, *288*, 373–382. [[CrossRef](#)]
18. Kuang, C.W.; Zeng, W.; Ye, H.; Li, Y.Q. A novel approach for fabricating NiO hollow spheres for gas sensors. *Physica E* **2018**, *97*, 314–316. [[CrossRef](#)]
19. Wei, Z.J.; Zhou, Q.; Lu, Z.R.; Xu, L.N.; Gui, Y.G.; Tang, C. Morphology controllable synthesis of hierarchical WO₃ nanostructures and C₂H₂ sensing properties. *Physica E* **2019**, *109*, 253–260. [[CrossRef](#)]
20. Xu, L.N.; Zeng, W.; Li, Y.Q. Synthesis of morphology and size-controllable SnO₂ hierarchical structures and their gas-sensing performance. *Appl. Surf. Sci.* **2018**, *457*, 1064–1071. [[CrossRef](#)]
21. Jiang, C.X.; Zhang, D.Z.; Yin, N.L.; Yao, Y.; Shaymurat, T.; Zhou, X.Y. Acetylene Gas-Sensing Properties of Layer-by-Layer Self-Assembled Ag-Decorated Tin Dioxide/Graphene Nanocomposite Film. *Nanomaterials* **2017**, *7*, 278. [[CrossRef](#)] [[PubMed](#)]
22. Zhu, L.; Li, Y.Q.; Zeng, W. Enhanced ethanol sensing and mechanism of Cr-doped ZnO nanorods: Experimental and computational study. *Ceram. Int.* **2017**, *43*, 14873–14879. [[CrossRef](#)]
23. Xing, X.X.; Yang, Y.; Yan, Z.Y.; Hu, Y.; Zou, T.; Wang, Z.D.; Wang, Y.D. CdO-Ag-ZnO nanocomposites with hierarchically porous structure for effective VOCs gas-sensing properties. *Ceram. Int.* **2019**, *45*, 4322–4334. [[CrossRef](#)]
24. Drmosh, Q.A.; Hendi, A.H.; Hossain, M.K.; Yamani, Z.H.; Moqbel, R.A.; Hezam, A.; Gondal, M. UV-activated gold decorated rGO/ZnO heterostructured nanocomposite sensor for efficient room temperature H₂ detection. *Sens. Actuators B-Chem.* **2019**, *290*, 666–675. [[CrossRef](#)]

25. Karouei, S.F.H.; Moghaddam, H.M. P-p heterojunction of polymer/hierarchical mesoporous LaFeO₃ microsphere as CO₂ gas sensing under high humidity. *Appl. Surf. Sci.* **2019**, *479*, 1029–1038. [[CrossRef](#)]
26. Sun, G.J.; Kheel, H.; Park, S.; Lee, S.; Park, S.E.; Lee, C. Synthesis of TiO₂ nanorods decorated with NiO nanoparticles and their acetone sensing properties. *Ceram. Int.* **2016**, *42*, 1063–1069. [[CrossRef](#)]
27. Zhu, L.; Zeng, W.; Yang, J.D.; Li, Y.Q. One-step hydrothermal fabrication of nanosheet-assembled NiO/ZnO microflower and its ethanol sensing property. *Ceram. Int.* **2018**, *44*, 19825–19830. [[CrossRef](#)]
28. Bunpang, K.; Wisitsoraat, A.; Tuantranont, A.; Singkammo, S.; Phanichphant, S.; Liewhiran, C. Highly selective and sensitive CH₄ gas sensors based on flame-spray-made Cr-doped SnO₂ particulate films. *Sens. Actuators B-Chem.* **2019**, *291*, 177–191. [[CrossRef](#)]
29. Lu, Z.R.; Zhou, Q.; Xu, L.N.; Gui, Y.G.; Zhao, Z.Y.; Tang, C.; Chen, W.G. Synthesis and Characterization of Highly Sensitive Hydrogen (H₂) Sensing Device Based on Ag Doped SnO₂ Nanospheres. *Materials* **2018**, *11*, 492. [[CrossRef](#)]
30. Bai, S.; Fu, H.; Zhao, Y.; Tian, K.; Luo, R.; Li, D.; Chen, A. On the construction of hollow nanofibers of ZnO-SnO₂ heterojunctions to enhance the NO₂ sensing properties. *Sens. Actuators B-Chem.* **2018**, *266*, 692–702. [[CrossRef](#)]
31. Hu, J.; Yang, J.; Wang, W.D.; Xue, Y.; Sun, Y.J.; Li, P.W.; Lian, K.; Zhang, W.D.; Chen, L.; Shi, J.; et al. Synthesis and gas sensing properties of NiO/SnO₂ hierarchical structures toward ppb-level acetone detection. *Mater. Res. Bull.* **2018**, *102*, 294–303. [[CrossRef](#)]
32. Bai, S.L.; Liu, C.Y.; Luo, R.X.; Chen, A.F. Metal organic frameworks-derived sensing material of SnO₂/NiO composites for detection of triethylamine. *Appl. Surf. Sci.* **2018**, *437*, 304–313. [[CrossRef](#)]
33. Kim, J.H.; Lee, J.H.; Mirzaei, A.; Kim, H.W.; Kim, S.S. SnO₂ (n)-NiO (p) composite nanowires: Gas sensing properties and sensing mechanisms. *Sens. Actuators B-Chem.* **2018**, *258*, 204–214. [[CrossRef](#)]
34. Meng, D.; Liu, D.Y.; Wang, G.S.; Shen, Y.B.; San, X.G.; Li, M.; Meng, F.L. Low-temperature formaldehyde gas sensors based on NiO-SnO₂ heterojunction microflowers assembled by thin porous nanosheets. *Sens. Actuators B-Chem.* **2018**, *273*, 418–428. [[CrossRef](#)]
35. Zhou, Q.; Zeng, W. Shape control of Co₃O₄ micro-structures for high-performance gas sensor. *Physica E* **2018**, *95*, 121–124. [[CrossRef](#)]
36. Zhang, Y.X.; Zeng, W.; Li, Y.Q. Theoretical and experimental investigations on H₂ sensing properties of flower-like titanium dioxide. *Mater. Res. Bull.* **2018**, *107*, 139–146. [[CrossRef](#)]
37. Liu, H.C.; Zhou, Q.; Zhang, Q.Y.; Hong, C.X.; Xu, L.N.; Jin, L.F.; Chen, W.G. Synthesis, Characterization and Enhanced Sensing Properties of a NiO/ZnO p-n Junctions Sensor for the SF₆ Decomposition Byproducts SO₂, SO₂F₂, and SOF₂. *Sensors* **2017**, *17*, 913. [[CrossRef](#)] [[PubMed](#)]
38. Varshney, D.; Dwivedi, S. Synthesis, structural, Raman spectroscopic and paramagnetic properties of Sn doped NiO nanoparticles. *Superlattice. Microst.* **2015**, *86*, 430–437. [[CrossRef](#)]
39. He, J.; Jiao, W.L.; Zhang, L.; Feng, R. Preparation and gas-sensing performance of SnO₂/NiO composite oxide synthesized by microwave-assisted liquid phase deposition. *Particuology* **2018**, *41*, 118–125. [[CrossRef](#)]
40. Bai, S.L.; Liu, J.C.; Guo, J.; Luo, R.X.; Li, D.Q.; Song, Y.J.; Liu, C.C.; Chen, A.F. Facile preparation of SnO₂/NiO composites and enhancement of sensing performance to NO₂. *Sens. Actuators B-Chem.* **2017**, *249*, 22–29. [[CrossRef](#)]
41. An, X.; Yu, J.C.; Wang, Y.; Yu, X.; Zhang, G. WO₃ nanorods/graphene nanocomposites for high-efficiency visible-light-driven photocatalysis and NO₂ gas sensing. *J. Mater. Chem.* **2012**, *22*, 8525–8531. [[CrossRef](#)]
42. Mane, A.T.; Navale, S.T.; Sen, S.; Aswal, D.K.; Gupta, S.K.; Patil, V.B. Nitrogen dioxide (NO₂) sensing performance of p-polypyrrole/n-tungsten oxide hybrid nanocomposites at room temperature. *Org. Electron.* **2015**, *16*, 195–204.
43. Karmakar, N.; Fernandes, R.; Jain, S.; Patil, U.V.; Shimpi, N.G.; Bhat, N.V.; Kothari, D.C. Room temperature NO₂ gas sensing properties of p-toluenesulfonic acid doped silver-polypyrrole nanocomposite. *Sens. Actuators B-Chem.* **2017**, *242*, 118–126. [[CrossRef](#)]
44. Jain, S.; Karmakar, N.; Shah, A.; Shimpi, N.G. Development of Ni doped ZnO/polyaniline nanocomposites as high response room temperature NO₂ sensor. *Mat. Sci. Eng. B* **2019**, *247*, 114381. [[CrossRef](#)]
45. Haiduk, Y.S.; Khort, A.A.; Lapchuk, N.M.; Savitsky, A.A. Study of WO₃-In₂O₃ nanocomposites for highly sensitive CO and NO₂ gas sensors. *J. Solid. State. Chem.* **2019**, *273*, 25–31. [[CrossRef](#)]

46. Zhang, Y.J.; Zeng, W.; Li, Y.Q. Hydrothermal synthesis and controlled growth of hierarchical 3D flowerlike MoS₂ nanospheres assisted with CTAB and their NO₂ gas sensing. *Appl. Surf. Sci.* **2018**, *455*, 276–282. [[CrossRef](#)]
47. Barsan, N.; Weimar, U. Conduction model of metal oxide gas sensors. *J. Electroceram.* **2001**, *7*, 143–167. [[CrossRef](#)]
48. Sun, J.H.; Sun, L.X.; Bai, S.L.; Fu, H.; Guo, J.; Feng, Y.J.; Luo, R.X.; Li, D.Q.; Chen, A.F. Pyrolyzing Co/Zn bimetallic organic framework to form p-n heterojunction of Co₃O₄/ZnO for detection of formaldehyde. *Sens. Actuators B-Chem.* **2019**, *285*, 291–301. [[CrossRef](#)]



© 2019 by the authors. Licensee MDPI, Basel, Switzerland. This article is an open access article distributed under the terms and conditions of the Creative Commons Attribution (CC BY) license (<http://creativecommons.org/licenses/by/4.0/>).